CHAPTER 4

FOLDABLE CYLINDRICAL TUBES WITH HELICAL FOLDS

The rotationally symmetric design of the origami stent graft described in Chapter 3 provides compact folding. But it has low radial stiffness because the longitudinal folds coincide with the collapse mechanism when the tube fails under radial pressure. A general approach to improve the radial stiffness is to replace longitudinal folds with helical ones.

Section 4.1 introduces basic concepts of the helical folds for cylindrical tubes. Advantages of the helical folds are discussed. In Section 4.2, the radius of the tube during deployment is defined and analysed. To understand the deployment process, the fold-shorting during deployment is calculated.

In order to obtain the optimum helical fold design, i.e. the optimum locations for the helical folds, the buckling of a thin-walled tube under torsion is considered. When a thin-walled tube buckles, a pattern of peaks and valleys forms on the structure. This buckling pattern is utilised to define the position of the helical folds so that the cylindrical tube can be easily folded and unfolded by twisting the tube. Section 4.3 finds the buckling pattern for a thin-walled tube using analytical solutions. The buckling pattern on a cardboard model under torsion is examined. In Section 4.4, the intentional helical folds of the foldable cylindrical tube are compared with the buckling patterns to establish a link between these parameters. Section 4.5 concludes this chapter.

4.1 Helical folds

Helical folds can be easily introduced by adjusting the joining positions of the left and right longitudinal edges of a developed tube surface. Figure 4.1(a) shows the surface of a foldable cylindrical tube with helical folds. It is based on rectangular elements where $\alpha_1 = \alpha_2 = 45^{\circ}$. To form a cylindrical tube with helical folds the horizontal opposite edges of the sheet, i.e., section a_2-a_3 and b_1-b_2, etc., are joined together. In this case there are 6.5 elements in one turn circle of a helix. Always a half element needs to be added at the end of each full circumference to allow connection of the left and right edges.

The major helical folds are denoted as H_A and H_B. They are orthogonal to one another as shown in Figure 4.1(a). Figures 4.1(b) and (c) show perspective views of the cylindrical tube in the unfolded and folded configurations. H_A is a single long fold which spirals around the circumference of the tube, while, H_B runs diagonally from one open end to the other.

The number of H_A and H_B type helices can vary. A foldable cylindrical tube with more than one H_A type helix can be made by adjusting the joining position of the left and right edges of the sheet shown in Figure 4.1(a). Figure 4.2 shows the development of the model with two helices, in which the opposite edges of the sheet a_3-a_4 and b_1-b_2, etc. are joined together. Photographs of the foldable cylinders with two and three helices in fully folded and expanded configurations are shown in Figures 4.3(a) and (b). The separate helices are shown in different colours. The number of H_B type of helices depends on the number of element *m*.

Helical folds bring a number of important advantages for the stent graft. Firstly, as shown in Figure 4.1(b), H_A type helices connect all of the elements like ribbons, enabling the folding and expansion processes to be synchronised among the elements. Secondly, the helical folds provide greater radial stiffness in the expanded configuration of the tube because H_B type folds no longer coincide with the collapsed hinge lines of the tube under external radial pressure. The stent graft will be permitted to collapse only under torsion at both ends. Since torsional loadings are rare in the human body, i.e. oesophageal and aorta, the stent graft will not collapse easily.

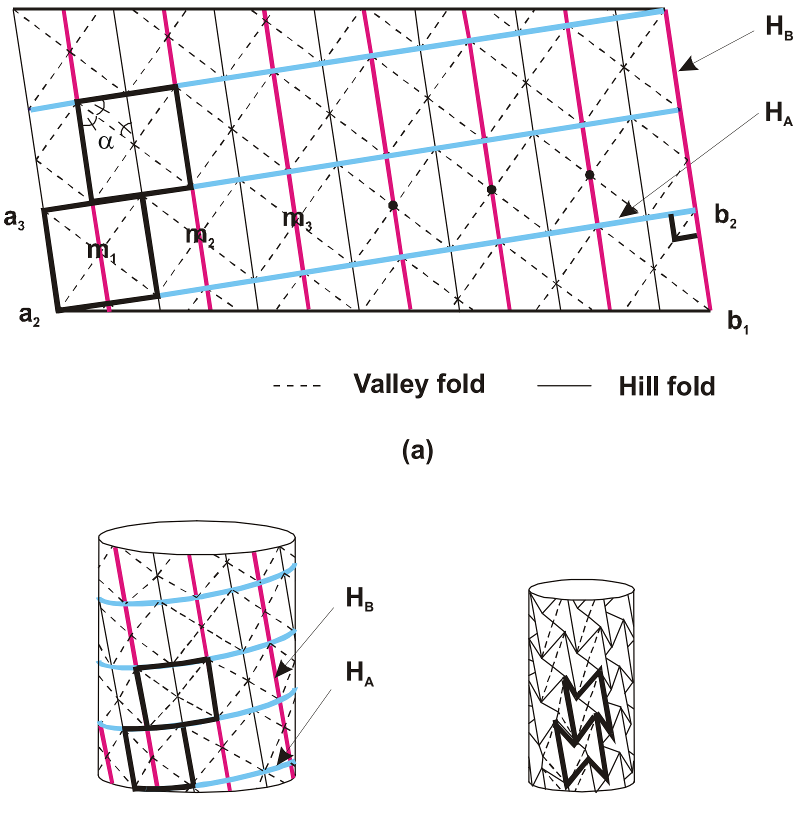

(a)

(b)

(c)

Figure 4.1 (a) Development of a helical foldable cylindrical tube.
(b) and (c) perspective view of the tube in its unfolded and folded configurations.

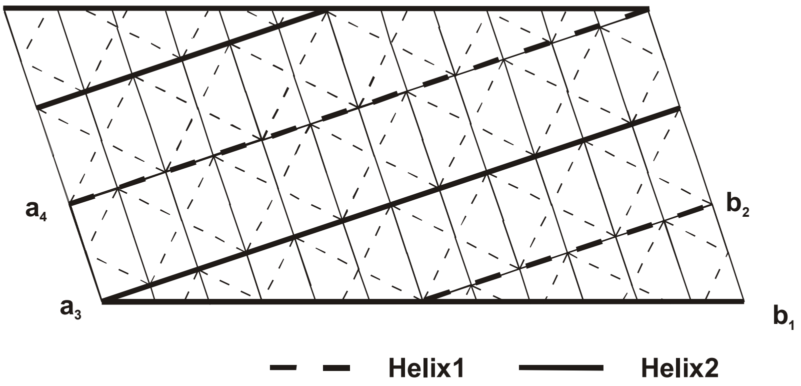

Figure 4.2 Development of a foldable tube with two H_A type helices.

a_3-a_4 and b_1-b_2 are jointed together to form a tube.

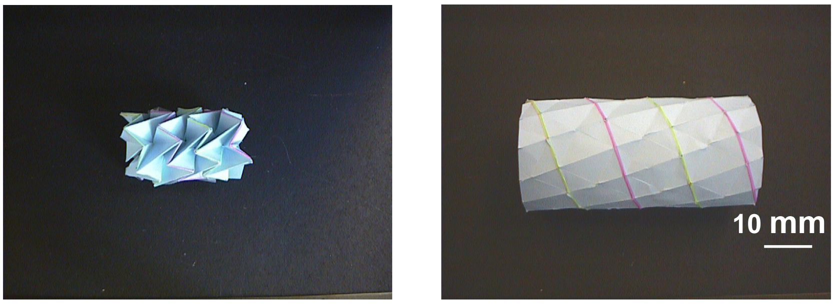

Fully folded **Fully expanded**

(a)

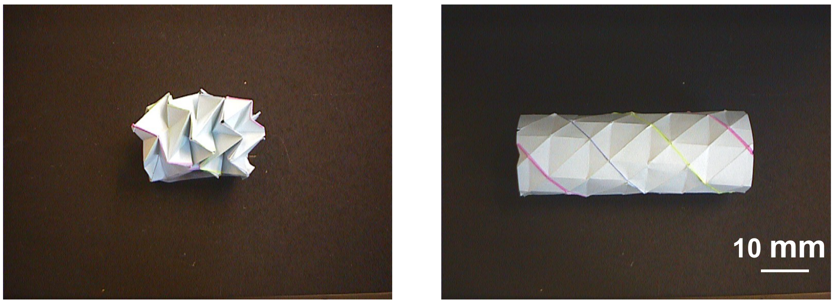

Fully folded **Fully**

(b)

Figure 4.3 Photographs of foldable cylindrical tubes with
(a) two and (b) three helical folds.

4.2 Geometry of the helical-type foldable cylindrical tube

4.2.1 Helical angle

Figure 4.4 shows the configuration of a foldable cylindrical tube with helical folds during deployment. The typical element is identical to that described in Section 3.2. The angles of H_A and H_B folds with respect to the horizontal base line are denoted as β_A and β_B, respectively. Note that β_A and β_B vary during deployment because both the length and diameter of the tube alter. However, H_A and H_B folds remain orthogonal to one another, and $a_2b_2'$and b_1b_2 intersect at b_2'. Hence, β_A is:

$$\beta_A = \arctan\left(\frac{b_1b_2'}{a_2b_2'}\right) \tag{4.1}$$

$$\beta_B = \frac{\pi}{2} - \beta_A \tag{4.2}$$

in which

$$b_1b_2' = b_1b_2 - b_2b_2' \tag{4.3}$$

$$a_2b_2' = (2m+1) \times \frac{AC}{2} \tag{4.4}$$

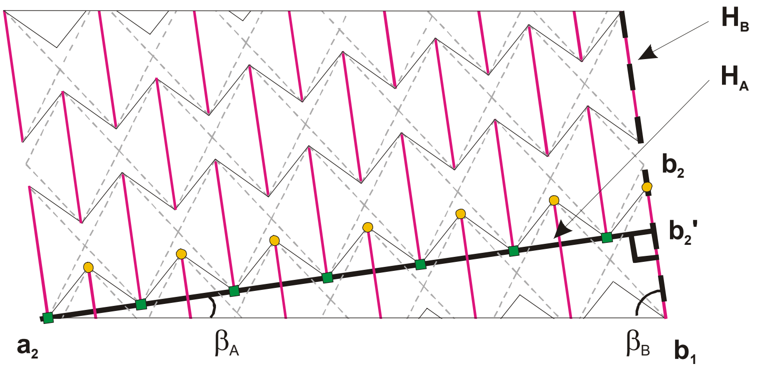

Figure 4.4 Configuration of the foldable cylindrical tube with helical folds during deployment.

where b_1b_2 has been calculated as AD in Equation (3.20) and b_2b_2' is as O'_2Q in Equation (3.65). m is the number of elements along a_2b_2'. AC has been calculated in Equation (3.14). Therefore, Equations (4.3) and (4.4) become

$$b_1b_2' = \frac{2l}{\tan\alpha_1} - \frac{l\sin 2\alpha_1\cos^2\theta}{1-\sin^2\alpha_1\sin^2\theta} - \frac{l}{\tan(\alpha_1+\alpha_2)}\frac{\cos^2\alpha_1 - \sin^2\alpha_1\cos^2\theta}{1-\sin^2\theta\sin^2\alpha_1}$$

$$= l\left[\frac{2\tan(\alpha_1+\alpha_2)\cos^2\alpha_1 - \sin\alpha_1\cos\alpha_1 + \sin^2\alpha_1\tan\alpha_1\cos\theta}{\tan\alpha_1\tan(\alpha_1+\alpha_2)(1-\sin^2\theta\sin^2\alpha_1)}\right] \tag{4.5}$$

$$a_2b_2' = (2m+1)l\sin\theta \tag{4.6}$$

Substituting Equations (4.5) and (4.6) into Equation (4.1) gives

$$\beta_{\mathrm{A}} = \arctan\left[\frac{2\tan(\alpha_1+\alpha_2)\cos^2\alpha_1 - \sin\alpha_1\cos\alpha_1 + \sin^2\alpha_1\tan\alpha_1\cos^2\theta}{(2m+1)\sin\theta\tan\alpha_1\tan(\alpha_1+\alpha_2)(1-\sin^2\alpha_1\sin^2\theta)}\right] \tag{4.7}$$

Figure 4.5 shows the results of the helical angle β_{A} versus deployable angle θ when $m = 4$, 6 and 12 and $\alpha_1 = \alpha_2 = 45^{\circ}$. In all cases, β_{A} decreases until θ reaches 55° and then increases. β_{A} becomes smaller if m is large.

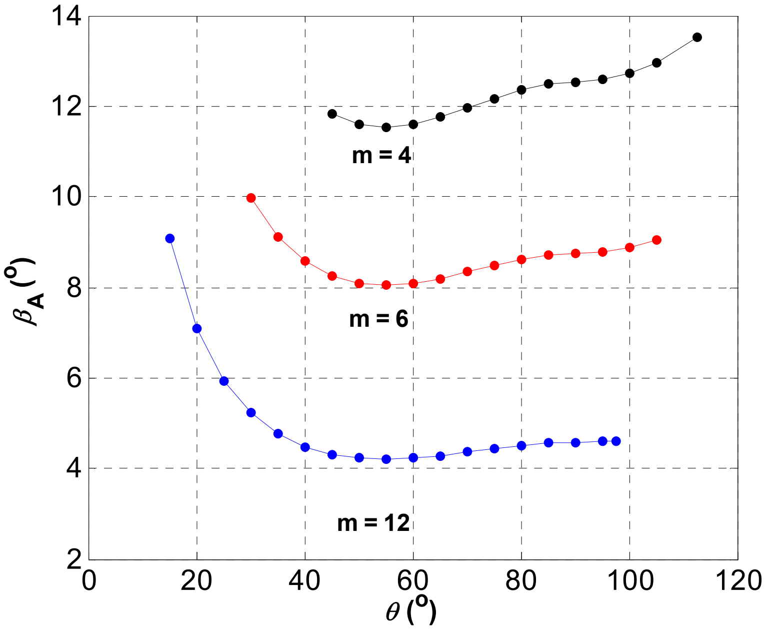

Figure 4.5 β_A **with various** θ **for** m **= 4, 6 and 12 when** $\alpha_1 = \alpha_2 = 45°$**.**

4.2.2 Radius

For simplicity, consider the tube consisting of the rectangular elements, i.e., $\alpha_1 + \alpha_2 = 90^{\circ}$ as described in Section 3.2. Figure 4.6(a) shows the element of the tube in the local coordinate system of (x', y', z'). Because of the arrangement of the elements, two coordinate systems are introduced. Figures 4.6(b) and (c) show a 3-dimensional schematic and top-view of the cylindrical tube in (X, Y, Z) coordinates, respectively. The distance from the Z axis of the model to nodes B and A are denoted as R_{o1} and R_{o2}, respectively, and R_{o1} and R_{o2} are obtained as follows.

Firstly, nodes A and B are defined in the local coordinate system of (x', y', z'). From Figure 4.6(a), these are given as A (0, 0, 0) and B ($O'B$, $AC/2$, $O'Q$) where AC, $O'B$ and $O'Q$ have been calculated in Equations (3.14), (3.24) and (3.42).

Secondly, we transform A and B from (x', y', z') to (X, Y, Z) coordinate systems. Nodes A and B are rotated by β_A about the x' axis and then by ϕ about the z' axis. Then,

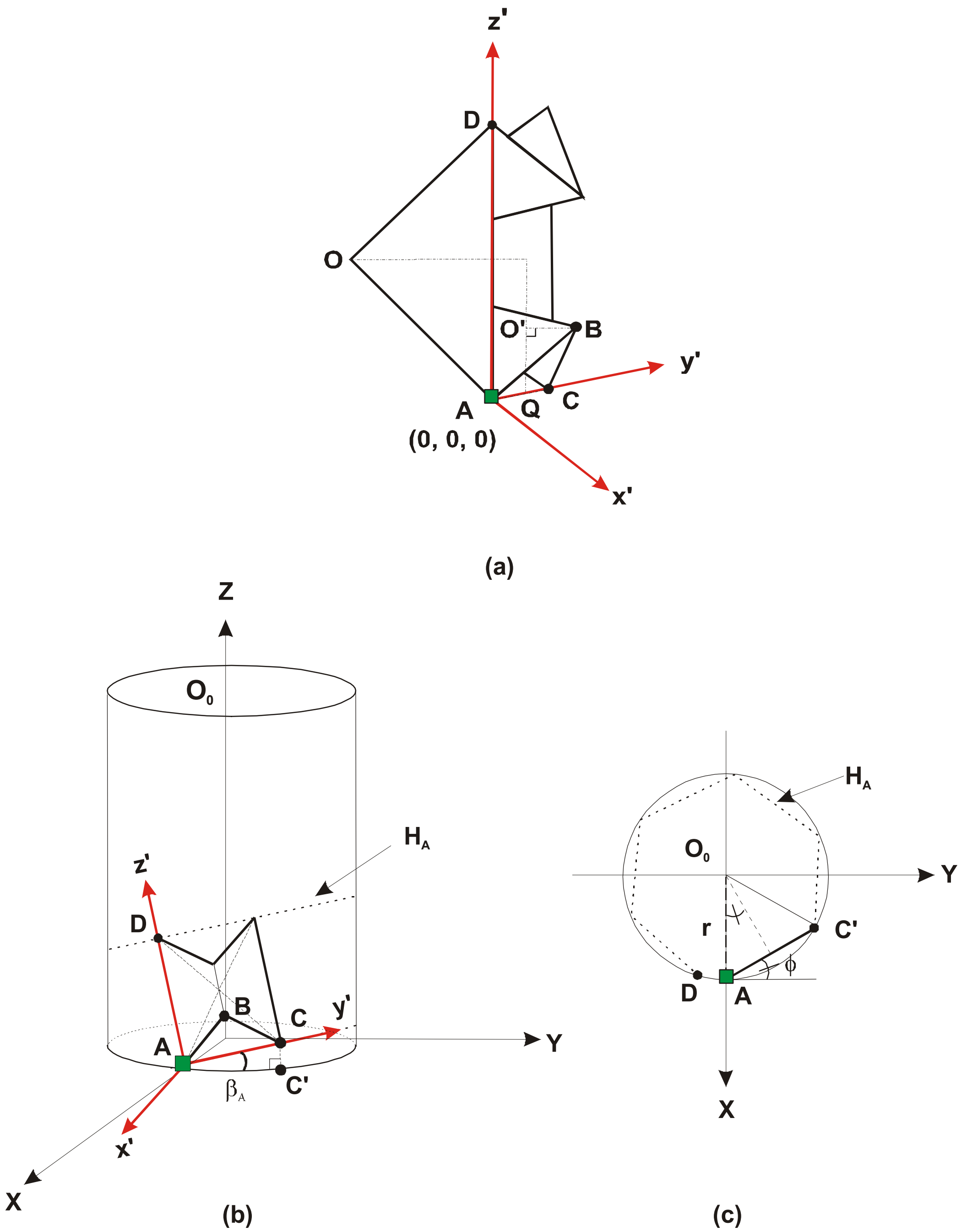

(a)

(b)

(c)

Figure 4.6 (a) Element (x', y', z') coordinates; (b) foldable cylindrical tube with helical folds and (c) its top's view in (X, Y, Z) coordinates.

they are translated by r in the X axis where r is the radius of the tube, also shown in Figure 4.6(c). The rotation matrix M is

$$[M]=\begin{bmatrix}\cos\phi & -\sin\phi & 0\\ \sin\phi & \cos\phi & 0\\ 0 & 0 & 1\end{bmatrix}\begin{bmatrix}1 & 0 & 0\\ 0 & \cos\beta_{\mathrm{A}} & -\sin\beta_{\mathrm{A}}\\ 0 & \sin\beta_{\mathrm{A}} & \cos\beta_{\mathrm{A}}\end{bmatrix}=\begin{bmatrix}\cos\phi & -\sin\phi\cos\beta_{\mathrm{A}} & \sin\phi\sin\beta_{\mathrm{A}}\\ \sin\phi & \cos\phi\cos\beta_{\mathrm{A}} & -\cos\phi\sin\beta_{\mathrm{A}}\\ 0 & \sin\beta_{\mathrm{A}} & \cos\beta_{\mathrm{A}}\end{bmatrix} \tag{4.8}$$

Therefore, the transformation is

$$\begin{bmatrix}X\\ Y\\ Z\end{bmatrix}=[M]\begin{bmatrix}x'\\ y'\\ z'\end{bmatrix}+\begin{bmatrix}r\\ 0\\ 0\end{bmatrix} \tag{4.9}$$

ϕ is equal to $\angle AO_{\mathrm{o}}C'/2$, see Figure 4.6(c). There is

$$r\sin\phi=\frac{AC'}{2} \tag{4.10}$$

where

$$AC'=AC\cos\beta_{\mathrm{A}}=2l\sin\theta\cos\beta_{\mathrm{A}} \tag{4.11}$$

In Figure 4.4, because

$$2\pi r=a_2b_1 \tag{4.12}$$

where

$$a_2b_1=\frac{a_2b_2'}{\cos\beta_{\mathrm{A}}}=\frac{(2m+1)l\sin\theta}{\cos\beta_{\mathrm{A}}} \tag{4.13}$$

due to Equation (4.6). Therefore,

$$r=\frac{(2m+1)l\sin\theta}{2\pi\cos\beta_{\mathrm{A}}} \tag{4.14}$$

Substituting Equations (4.14) and (4.11) into (4.10) gives

$$\phi = \arcsin\left(\frac{2\pi\cos^2\beta_{\mathrm{A}}}{2m+1}\right) \tag{4.15}$$

Once r and ϕ are known, the positions of nodes A and B in (X, Y, Z) coordinate systems can be calculated using Equation (4.8) and (4.9), leading to R_{o1} and R_{o2}.

For general elements shown in Figure 3.11, node B' replaces B. Therefore, from Figure 3.13 O'_2B' and O'_2Q need to replace $O'B$ and $O'Q$, respectively. O'_2B' is derived as follows

$$O'_2B' = O'B - HB \tag{4.16}$$

where $O'B$ has been calculated in Equation (3.24) and

$$HB = BB'\cos\varphi \tag{4.17}$$

in which BB' and $\cos\varphi$ have been calculated in Equations (3.55) and (3.54), therefore,

$$HB = \frac{l}{\tan(\alpha_1+\alpha_2)}\frac{\sin 2\alpha_1\cos\theta}{1-\sin^2\theta\sin^2\alpha_1} \tag{4.18}$$

and

$$O'_2B' = l\cos\theta\frac{\cos^2\alpha_1-\sin^2\alpha_1\cos^2\theta}{1-\sin^2\theta\sin^2\alpha_1} - \frac{l}{\tan(\alpha_1+\alpha_2)}\frac{\sin 2\alpha_1\cos\theta}{1-\sin^2\theta\sin^2\alpha_1} \tag{4.19}$$

O'_2Q has been calculated in Equation (3.65). Again, the position of nodes A and B in the global coordinate system (X, Y, Z) can be obtained.

4.2.3 Deformation

In Section 3.3 (Figure 3.7), it is found that there is a mismatch between radii of the element when they are connected in the longitudinal direction. The same occurs in the deployment of the tubes with helical folds.

The length between the nodes E_2 or A_1 and F_2 or B_1 has been denoted as l_a

$$l_a = \left[\left(R_{E2A1} \cos \delta_{E2A1} - R_{F2B1} \cos \delta_{F2B1} \right)^2 + \left(R_{E2A1} \sin \delta_{E2A1} - R_{F2B1} \sin \delta_{F2B1} \right)^2 + \left(Z_{E2A1} - Z_{F2B1} \right)^2 \right]^{\frac{1}{2}} \quad (4.20)$$

In the cylindrical coordinate system, the coordinate of nodes E_2 or A_1 are (R_{E2A1}, δ_{E2A1}, Z_{E2A1}) and those of nodes F_2 or B_1 are (R_{F2B1}, δ_{F2B1}, Z_{F2B1}) where R_{E2A1} and R_{F2B1} are $(R_{o1}+R_{o2})/2$; $\delta_{E2A1} = 0^{\circ}$; $\delta_{F2B1} = \arctan(Y/X)$ in which Y and X are the coordinates of node B calculated in Section 4.2.2. The difference between Z_{E2A1} and Z_{F2B1} is the value of the Z coordinate of node B as follows

$$Z_{E2A1} - Z_{F2B1} = Z = \frac{AC}{2} \sin \beta_A + O'_2 Q \cos \beta_A \quad (4.21)$$

Substituting Equations (3.14) and (3.65) into (4.21)gives

$$Z_{E2A1} - Z_{F2B1} = l \left\{ \begin{array}{l} \sin\theta \sin\beta_A + \\ \dfrac{\cos\beta_A}{1 - \sin^2\theta \sin^2\alpha_1} \left(\sin 2\alpha_1 \cos^2\theta + \dfrac{\cos^2\alpha_1 - \sin^2\alpha_1 \cos^2\theta}{\tan(\alpha_1 + \alpha_2)} \right) \end{array} \right\} \quad (4.22)$$

The mismatch is considered when l is replaced to $l_a \sin(\alpha_1 + \alpha_2)$ in Equation (4.22).

Consequently, Equation (4.20) becomes

$$l_a = \left\{ \frac{1}{1 - \sin^2(\alpha_1 + \alpha_2) S^2} \times \frac{(R_{o1} + R_{o2})^2}{2} \left[1 - \cos(\arctan(Y/X)) \right] \right\}^{\frac{1}{2}} \quad (4.23)$$

in which

$$S = \sin\theta \sin\beta_{\mathrm{A}} + \frac{\cos\beta_{\mathrm{A}}}{1-\sin^2\theta\sin^2\alpha_1}\left(\sin 2\alpha_1 \cos^2\theta + \frac{\cos^2\alpha_1 - \sin^2\alpha_1\cos^2\theta}{\tan(\alpha_1+\alpha_2)}\right) \tag{4.24}$$

4.2.4 Results and discussion

Similar to Chapter 3, two models are considered in which $\alpha_1 = \alpha_2 = 45^{\circ}$ and $\alpha_1 = \alpha_2 = 30^{\circ}$. For convenience, they are called Models 3 and 4.

- **Radii**

Figures 4.7(a) and (b) show the radii R_{o1} and R_{o2} of Models 3 and 4 normalised with respect to the length l versus the deployment angle, θ, when m is 6. In Model 3, R_{o1} is greater than R_{o2} until θ is 73°. In Model 4, R_{o1} is almost always smaller than R_{o2}.

The ratio of R_{o1} in the fully folded configuration to R_{o1} in the fully expanded configuration is denoted as R^*, which is 51.5% and 53.2% for Models 3 and 4.

Figure 4.8 shows the relationship between R^* and m for Model 3. For comparison, the result for the foldable cylindrical tube without helical folds is also shown. Both curves are similar, and R^* decreases as m increases.

Figures 4.9(a) and (b) show the photographs of card models of Model 3 in its fully folded and expanded configurations when m is 4 and 6, respectively. It can be seen that the model with larger m can be folded more compactly because its radius in the fully expanded configuration is larger.

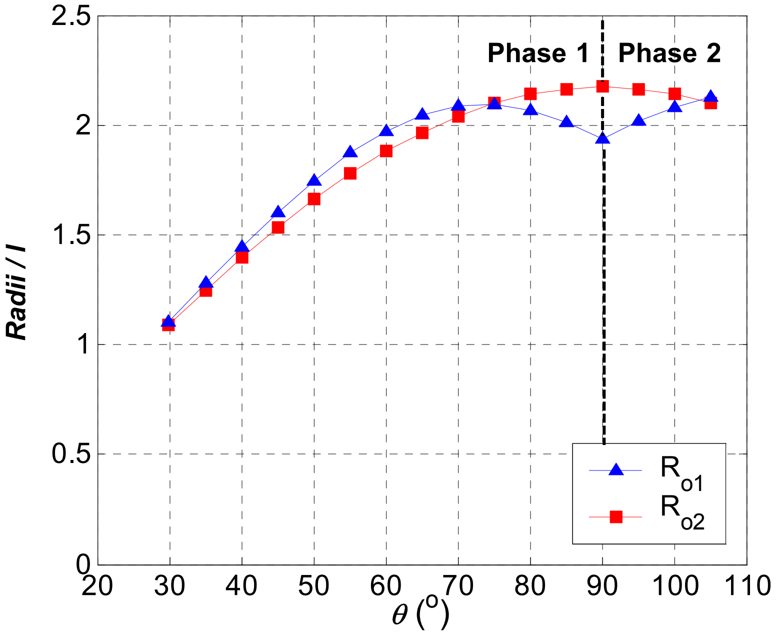

(a)

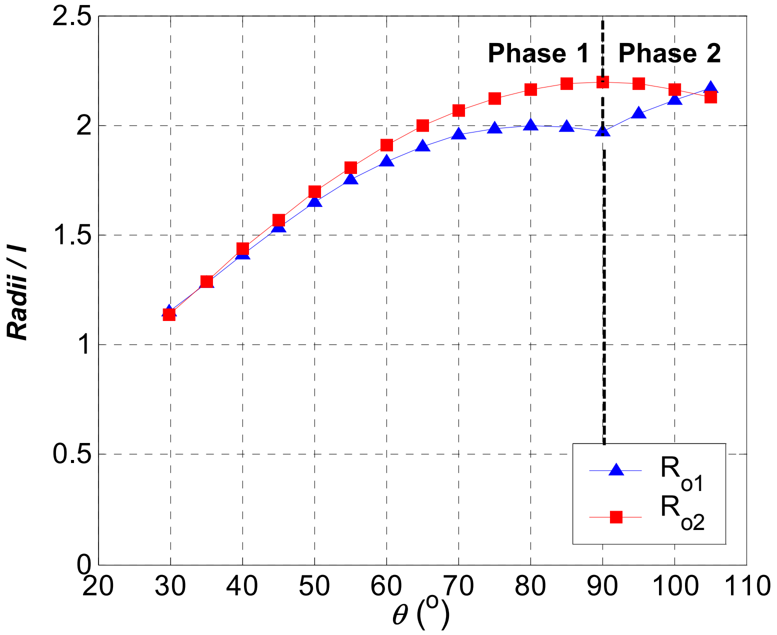

(b)

Figure 4.7 R_{o1} and R_{o2} vs. θ when m = 6. (a) Model 3 and (b) Model 4.

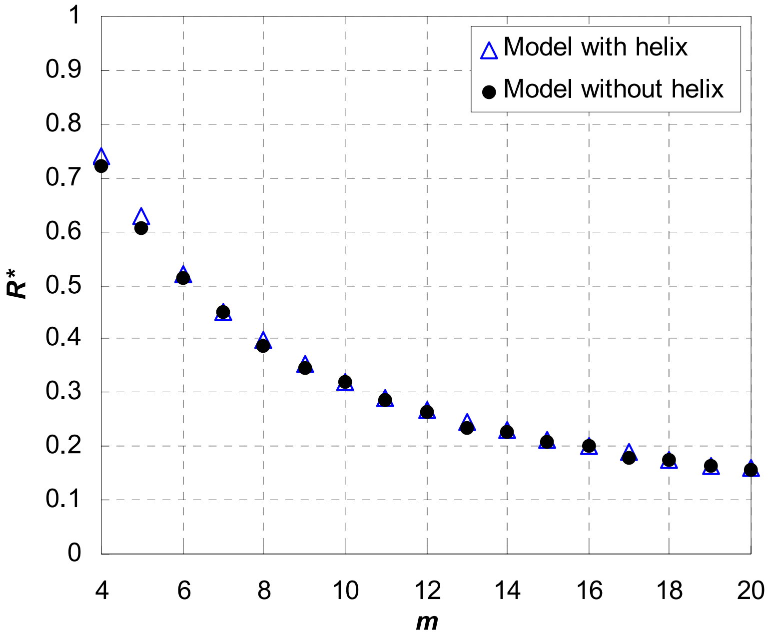

Figure 4.8 R^* vs. m for Model 3.

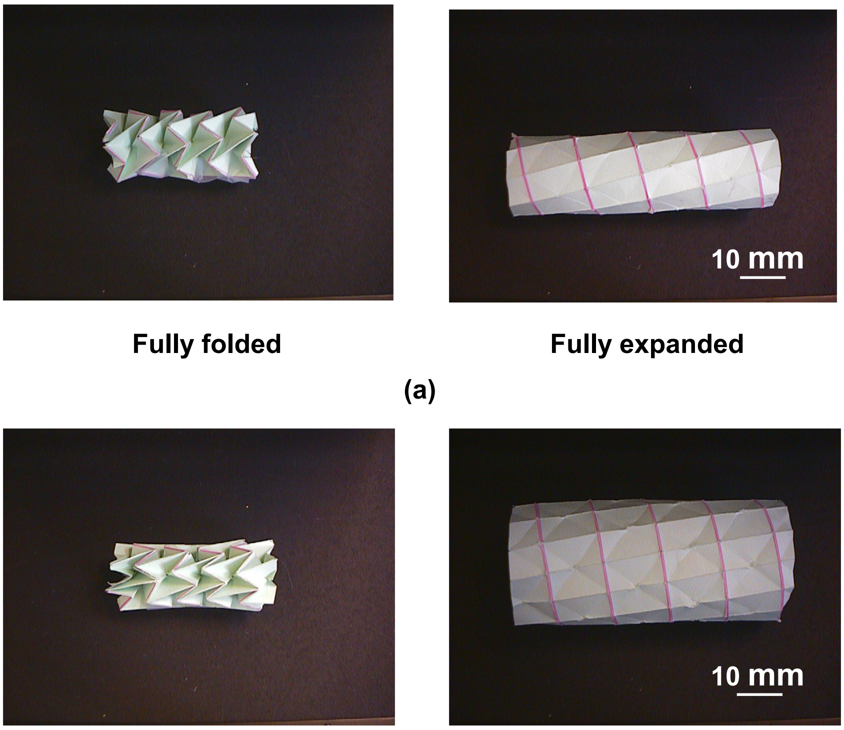

Fully folded

Fully expanded

(a)

Fully folded

Fully expanded

(b)

Figure 4.9 Photographs of Model 3 when (a) m = 4 and (b) m = 6.

- **Deformation**

Figures 4.10 shows a plot of l_a / l_o versus the deployment angle θ of Model 3 with helical folds for *m* of 6. For comparison, the results of the foldable cylindrical tube without helical folds are presented as well. It is noted that l_a becomes l_o and the structure becomes unstrained when $\theta = 73^\circ$ and $\theta = 103^\circ$. The deformations of the tube with helical folds are larger than those of the symmetric tube until $\theta = 73^\circ$ and then the difference between the foldable cylindrical tubes with and without helical folds become small.

Figures 4.11 (a) and (b) shows a plot of l_a / l_o versus the deployment angle θ with helical folds with *m* of 9 for Models 3 and 4, respectively. For Model 3, as *m* increases the deformations become smaller than the result shown in Figure 4.10. For Model 4, the deformation becomes very small until about $\theta = 55^\circ$ at the beginning of the first phase.

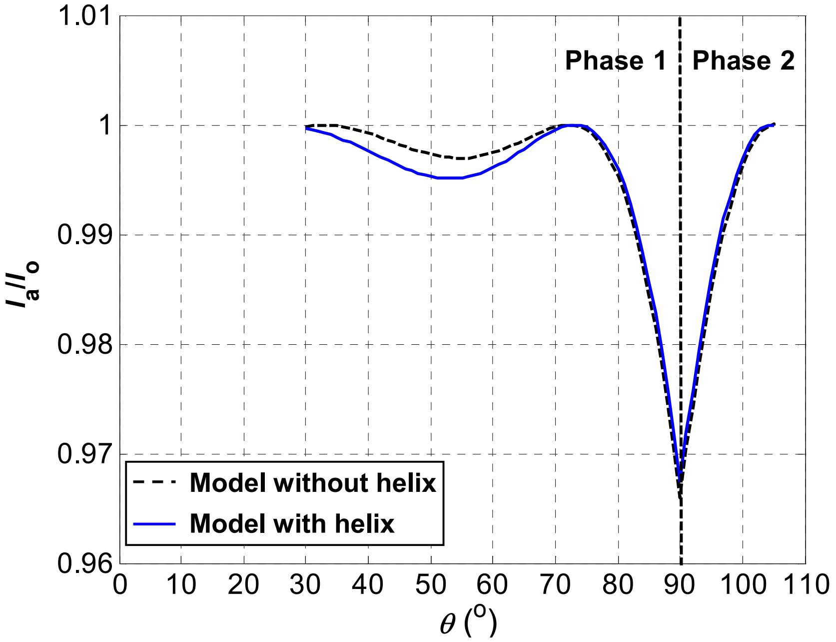

Figure 4.10 Plots of l_a/l_o vs. θ for Model 4 when *m* = 6. The data for similar models without helical folds are also included.

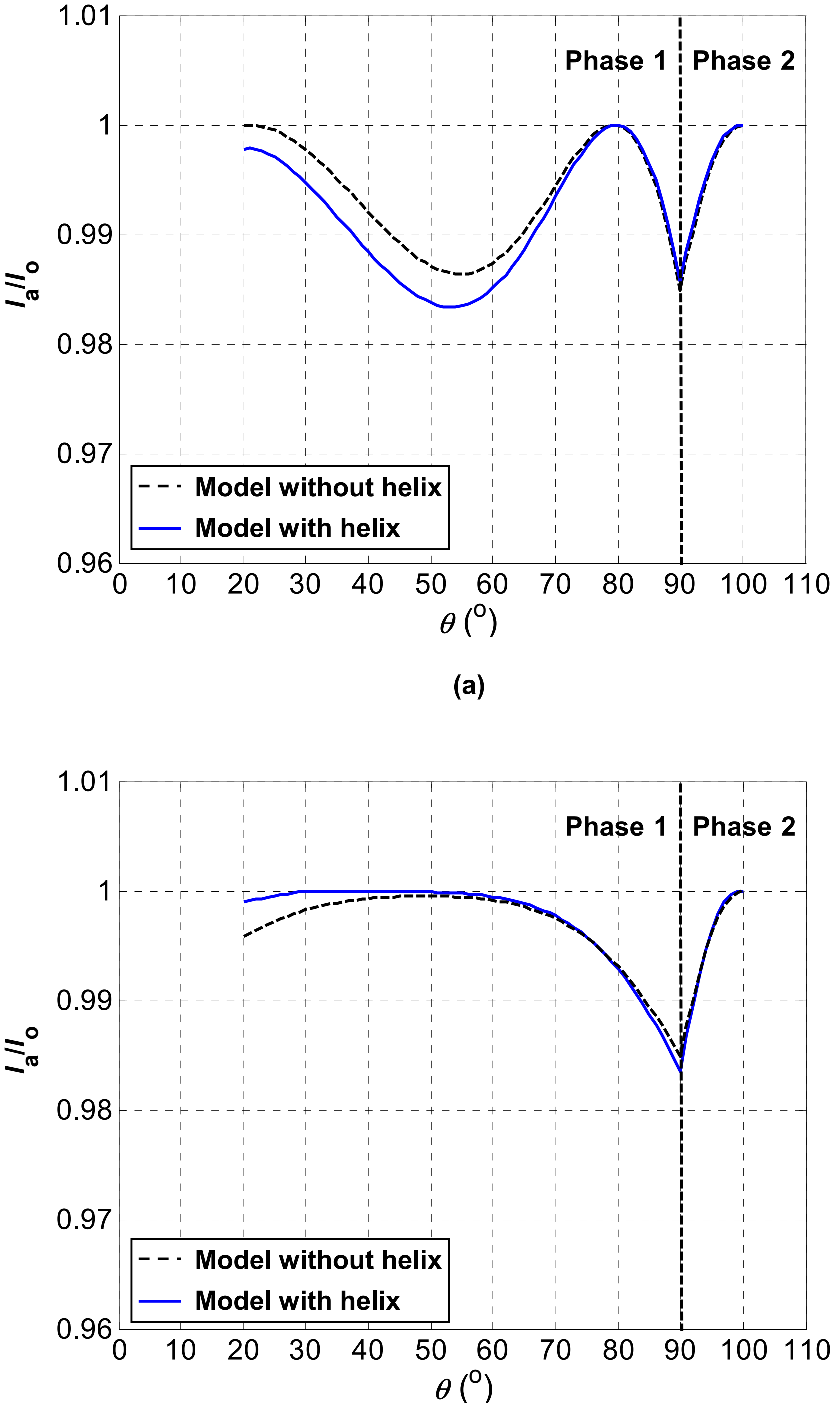

(a)

(b)

Figure 4.11 Plots of I_a/I vs. θ for foldable cylindrical tube with and without helical folds when $m = 9$, (a) Model 3 and (b) Model 4. The data for similar models without helical folds are also included.

4.3 Buckling patterns

In Section 4.1, H_B type folds sustain an angle β_B to the horizontal line (see Figure 4.4). These are similar to the folds in the buckling failure pattern of a thin-walled tube under torsion. The forthcoming sections consider the buckling pattern to optimise the locations of the helical folds in order to make folding a naturally efficient process.

4.3.1 Analytical results

When a perfect thin-walled tube is under torsion, it reaches a threshold after which it loses stability and buckles. Figure 4.12(a) shows a schematic diagram of a buckled tube. The bucking patterns contains peak and valley folds around the surface of the tube, which represent a wave in the cross-sectional view of the buckled tube shown in Figure 4.12(b). The peak folds are called the buckling lines. The angle between the buckling line and the x axis, shown in Figure 4.12(c), is denoted as δ_b.

The torsional buckling of a cylindrical shell was first studied by Donnell (Donnell 1933; Donnell 1951; Timoshenko and Gere 1961; Calladine 1983). Assume that the tube has a finite length L whose ends are supported in such a way that the radial displacement w is equal to zero. The displacement w in the radial direction at y can be assumed as:

$$w = W \sin\left(m_b \theta - \frac{m_b n_b y}{r} \right) \sin\left(\frac{y\pi}{L} \right) \tag{4.25}$$

where r is radius of the tube. m_b is the total number of the buckling lines and $\frac{1}{n_b}$ represents the slope of the buckling lines. From Equation (4.25), it is noted that the radial displacement w is sinusoidal in a circumferential direction with the buckling wave number m_b ($b = 1, 2, 3, \cdots$) at any cross-section positions where y is neither zero or L (see Figure 4.12b).

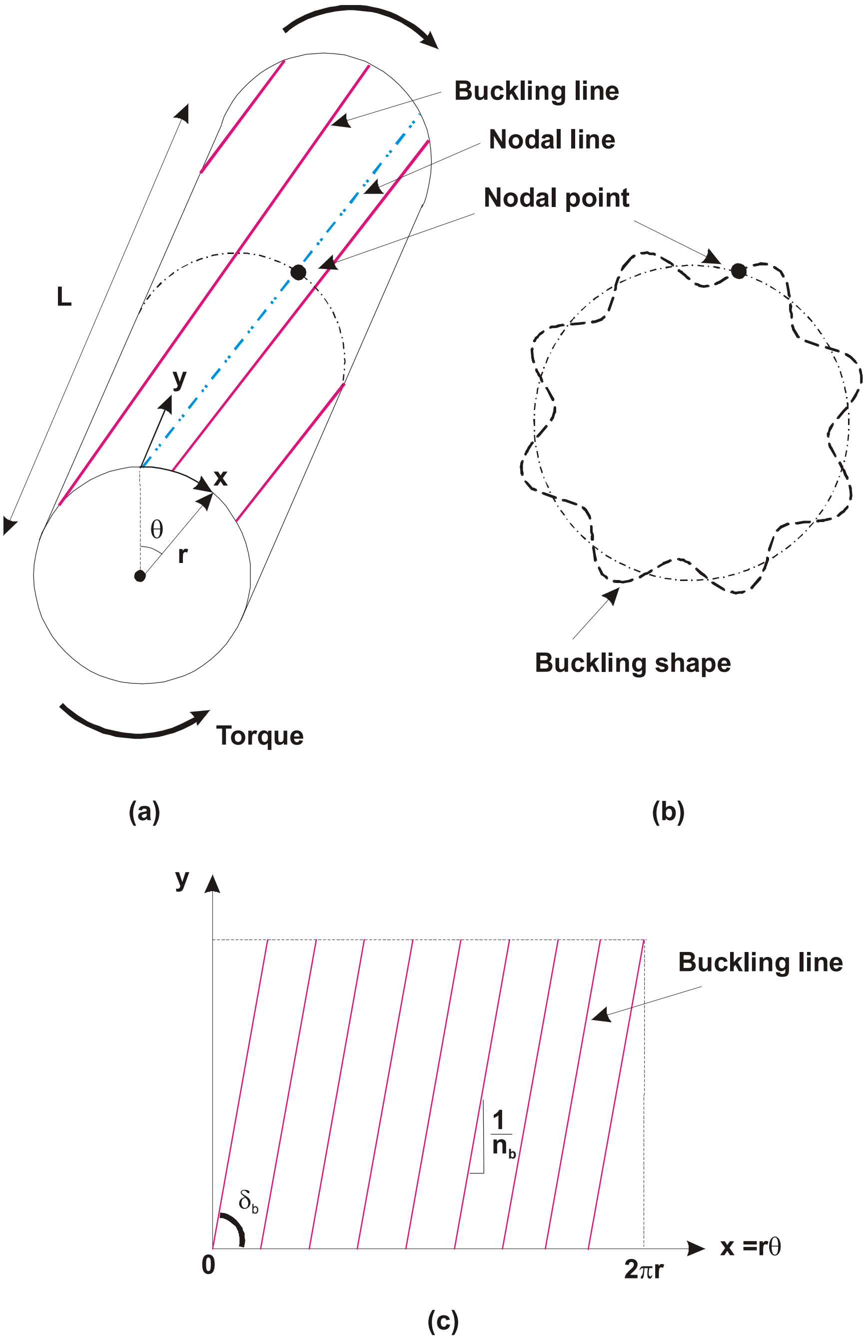

Figure 4.12 (a) Schematic diagram of a buckled tube, (b) cross-sectional view and (c) development of the tube with buckling lines.

From Equation (4.25), the nodal points where $w = 0$ (see Figure 4.12b) are formed when

$$m_{\mathrm{b}}\theta - \frac{m_{\mathrm{b}}n_{\mathrm{b}}y}{r} = k\pi \qquad (k = 0, 1, 2, \cdots) \tag{4.26}$$

Since $\theta = x/r$, Equation (4.26) can be rewritten

$$y = \frac{1}{n_{\mathrm{b}}}x - \frac{rk\pi}{m_{\mathrm{b}}n_{\mathrm{b}}} \tag{4.27}$$

which is the helical lines drawn on the cylindrical surface produced by connecting the nodal points in the longitudinal direction as shown in Figure 4.12(a). They are called nodal lines. From Equation (4.27) it is noted that $\frac{1}{n_{\mathrm{b}}}$ represents the slope of the nodal lines.

Since the buckling lines are parallel to the nodal lines, the buckling angle δ_{b} is consequently obtained by

$$\delta_{\mathrm{b}} = \tan^{-1}\frac{1}{n_{\mathrm{b}}} \tag{4.28}$$

Next, a buckling shear stress resultant N_{yx} is considered. Under pure torsion, the only non-zero stress resultant is N_{yx}. The total strain energy, which is involved in the distortion of the shell by both longitudinal stretching and circumferential bending, must be equal to the total energy supplied by the loading device. Thus, N_{yx} can be obtained using the energy method (Calladine 1983).

$$N_{yx}=\frac{r^2}{2n_\mathrm{b}m_\mathrm{b}{}^2}\left[\frac{m_\mathrm{b}{}^4Eth^2}{12r^4}+\left(\frac{n_\mathrm{b}{}^4}{r^2}+\frac{6n^2\pi^2}{m_\mathrm{b}{}^2L^2}+\frac{\pi^4r^2}{m_\mathrm{b}{}^4L^4}\right)Et\right] \tag{4.29}$$

where t is a thickness of the tube, and h is the effective thickness of the shell $h=t/\sqrt{1-\nu^2}$. E and ν are the Young's modulus and Poison's ratio, respectively. Equation (4.29) gives N_{yx} as a function of the two parameters n_b and m_b. Supposing that the value of m_b is fixed, N_{yx} can be minimised with respect to n_b, which is:

$$\frac{dN_{yx}}{dn_\mathrm{b}}=\left[-\left(\frac{m_\mathrm{b}{}^2h^2}{24r^2}+\frac{r^4\pi^4}{2m_\mathrm{b}{}^6L^4}\right)\frac{1}{n_\mathrm{b}{}^2}+\frac{3n_\mathrm{b}{}^2}{2m_\mathrm{b}{}^2}+\frac{3r^2\pi^2}{m_\mathrm{b}{}^4L^2}\right]Et=0 \tag{4.30}$$

Using the following notations:

$$u=n_\mathrm{b}{}^2,\ A=\frac{3}{2m_\mathrm{b}{}^2},\ B=\frac{3r^2\pi^2}{m_\mathrm{b}{}^4L^2},\ C=-\left(\frac{m_\mathrm{b}{}^2h^2}{24r^2}+\frac{r^4\pi^4}{2m_\mathrm{b}{}^6L^4}\right) \tag{4.31}$$

Equation (4.30) becomes

$$Au^2+Bu+C=0 \tag{4.32}$$

from which n_b can be solved.

$$u=n_\mathrm{b}{}^2=\frac{-B\pm\sqrt{B^2-4AC}}{2A} \tag{4.33}$$

Table 4.2 shows the values of δ_b and N_{yx} for various m_b calculated using Equations (4.33), (4.28) and (4.29). The length L, radius r and thickness t of the tube are taken as 60 mm, 12.7 mm and 0.025 mm, respectively. The Young's modulus E and

Poison ratio ν are 72 GPa and 0.3. Obviously, the shear stress N_{yx} becomes the smallest when $m_b = 9$, which is the number of buckling lines presented when the tube loses stability under torsion.

Using this method, we are able to identify m_b and δ_b for tubes of various dimensions. When thickness and length of the tube change, the results are given in Table 4.3 in which r is always 12.7 mm. It has been found that as L increases, m_b decreases but δ_b increases. It is also found that as t increases, m_b decreases. Table 4.4 shows m_b and δ_b with respect to various values of r when L = 60 mm and t = 0.025 mm. It is found that as r increases, m_b increases but δ_b decreases. These results will be used to find the optimal folding pattern of the helical-type foldable cylinder in Section 4.7.

Table 4.2 Buckling angle and the shear stress for various m_b when L = 60 mm, r = 12.5 mm and t = 0.025 mm.

m_b	δ_b (°)	N_{yx} (N/m)
3	84.98	5800.54
4	86.05	1451.57
5	86.15	593.00
6	85.34	376.87
7	84.02	310.80
8	82.62	289.22
9	81.30	287.44
10	80.05	294.93
11	78.87	308.11

Table 4.3 m_b and δ_b for tubes of various length and thickness.

***t* = 0.025 (mm)**			***t* = 0.08 (mm)**		
***L* (mm)**	**m_b**	**δ_b (°)**	***L* (mm)**	**m_b**	**δ_b (°)**
60	9	81.30	60	7	77.93
90	7	83.33	90	5	81.75
120	6	84.30	120	5	81.29
160	5	85.33	160	4	83.20
200	5	85.22	200	4	82.95

Table 4.4 m_b and δ_b for tubes of various r when L = 60 mm and t = 0.025 mm.

***r* (mm)**	**m_b**	**δ_b (°)**
6.4	5	83.46
9.5	7	82.43
12.7	9	81.30
15.9	10	81.73
19.1	12	80.79

4.3.2 Physical modelling

To verify the analytical results, a number of model tubes are prefabricated using cardboard. Figure 4.13 shows the schematic diagram of such a cylindrical tube. According to the results of Donnell's formula shown in Table 4.2, the buckling pattern consists of $m_b = 8$ folds at $\delta_b = 82.62^o$ when $L = 60$ mm, $t = 0.025$ mm. Three models are created in which folds are scored at $\delta_b = 82.62^o$, which is the same as the buckling angle, 60^o and 88^o. The length of the models is 60 mm and the number of the folds is 8. Wood bars are placed at each end of the tube to support the cardboard, and then the tubes are twisted by applying torques at both ends using hand motions.

Figures 4.14(a)-(c) shows photographs the three models taken after the twisting tests. When δ_b is the same as the bucking pattern (δ_b = 82.62°), the tube buckles and is twisted easily. When δ is larger than the buckling pattern (δ_b = 88°), the tube does not buckled at all. But it is damaged at one point. When δ_b is smaller than the buckling pattern (δ_b = 60°), only one end of the tube buckles. Although the boundary conditions of the cardboard models may not fit exactly to the assumption of the analyses, these simple tests indicates that the tube where the folds are created along the same angles as the natural buckling pattern (δ_b = 82.62°) is more easily buckled than the other tubes. Therefore, the physical models confirm the results of the analysis.

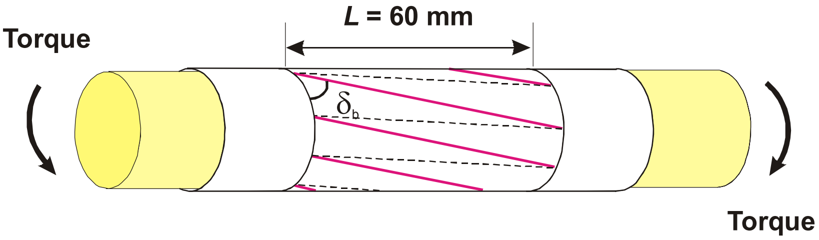

Figure 4.13 Schematic diagram of cylindrical tube with prefabricated folds.

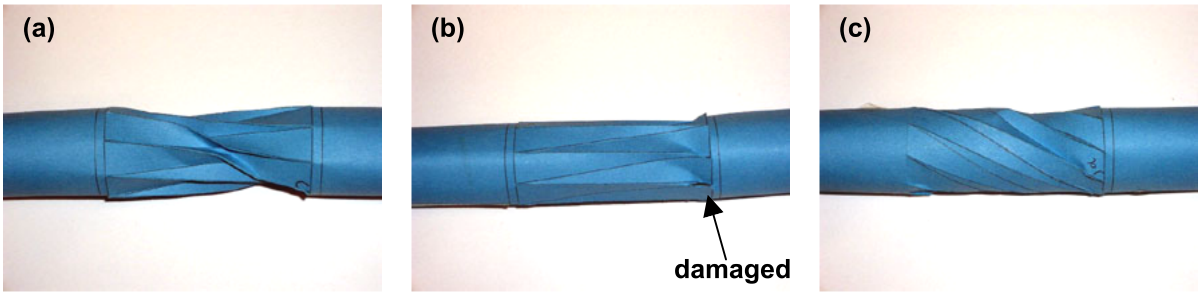

Figure 4.14 Twisted tubes with δ_b of (a) 82.62°, (b) 88° and (c) 60°.

4.4 Optimum folding patterns

In order to enable a helical-type cylindrical tube to be folded up easily, an optimum pattern of the helical folds needs to be found. Based on the previous sections, it is obvious that utilisation of the buckling patterns will provide a folding pattern which can be folded using the least energy consumption.

In the geometric analysis, the helical folds are determined by β_B, which is the angle between the H_B type helical folds and horizontal base line, and the element number m. The analysis does not consider the effect of the length, diameter and thickness of the tube. On the other hand, the buckling patterns are determined by the angle δ_b and m_b. They are related to the length and thickness of the tube. The values of δ_b and m_b are compared with the values of β_B in the fully expanded configuration of the tube and m, respectively. From the comparison, the suitable values of m and the design of the element, such as α_1 and α_2, for the helical origami stent graft are found.

Now consider a set of curves shown in Figure 4.15 for various α_1. They are obtained from the geometric analysis using Equation (4.2), in which it is assumed that $\alpha_2 = \alpha_1$. Each point along the curves represents a geometrically feasible design. If we also consider the length, radius and thickness of the tube, the buckling analysis indicates that δ_b = 81.3° and m_b = 9 when L = 60 mm, r = 12.7 mm and $t = 0.025$ mm, (see Table 4.3). The corresponding point is marked in Figure 4.15. It is obvious that the curve closest to the point is that of $\alpha_1 = \alpha_2 = 30°$. Therefore, for example, if a helical stent graft has $L = 60$ mm, $r = 12.7$ mm and $t = 0.025$ mm, the element with $\alpha_1 = 30^\circ$ and $m = 9$ should be used to achieve the optimal helical folding pattern. As shown in Figure 4.15, as L increases, the buckling pattern m_b decreases and δ increases. Therefore for a stent graft with larger values of L, m should also decrease. However, as shown in Figure 4.8 a smaller value for m led to a less complete compaction of the stent graft, which is less suitable for the stent design. Furthermore if L becomes longer than 160 mm, the calculated values of m and β_B, and also α_1 do not match the buckling pattern.

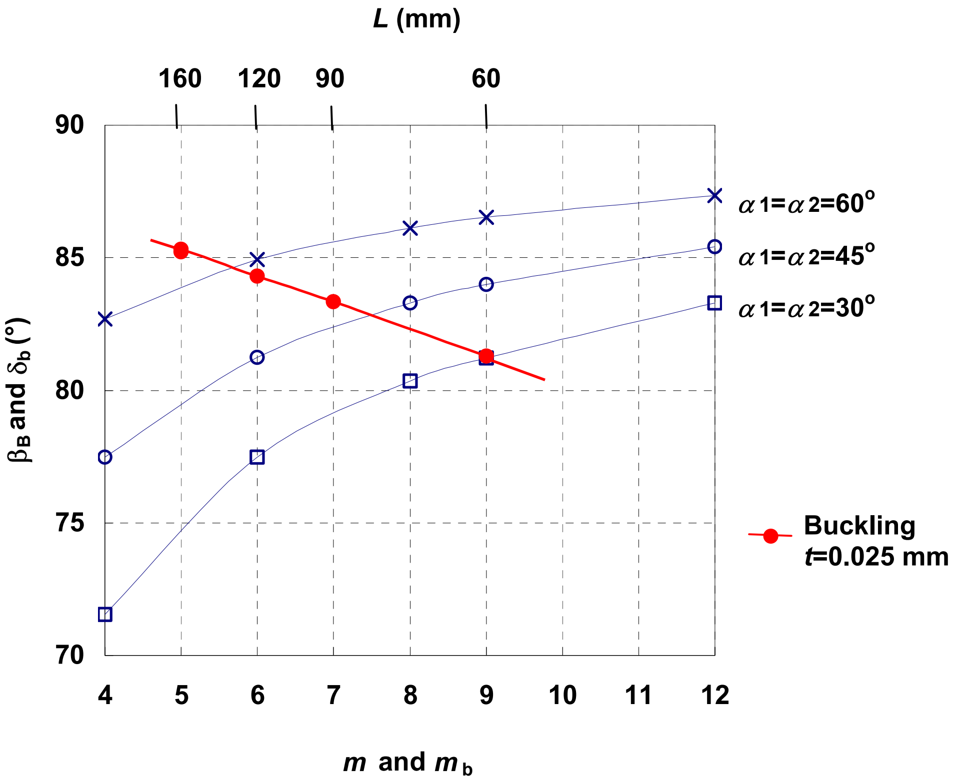

Figure 4.15 Geometric relationship of β_B vs. *m* of the helical-type foldable cylinders and the relationship of δ_b and m_b of buckling pattern for various *L* when *r* = 12.7 mm and t = 0.025 mm.

Figure 4.16 shows the buckling patterns δ and m_b for various radii when t = 0.025 mm and L = 60 mm which can be obtained from Table 4.4 and are shown as solid square symbols. The optimum helical folding pattern for the helical stent graft can be designed by matching those results. However, as shown in Figure 4.16 as radii decrease, the buckling pattern m_b decreases and δ increases, which will conflict results of m and β_B, and also α_1.

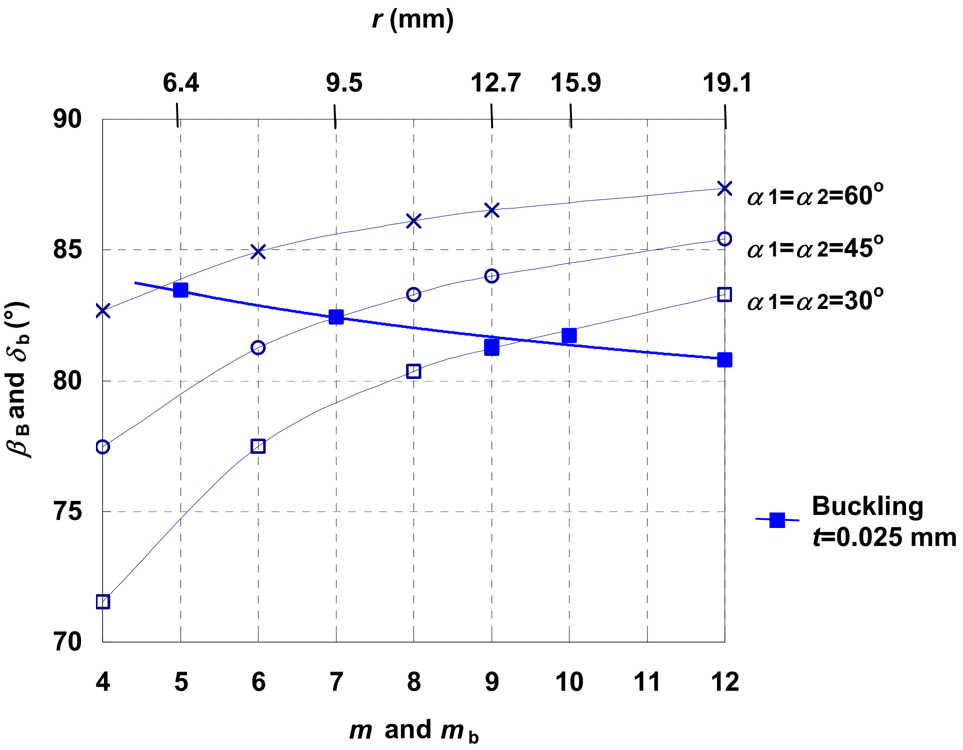

Figure 4.16 Geometric relationship of β_B vs. *m* of the helical-type foldable cylinders and the relationship of δ_b and m_b of buckling pattern for various *L* when *L*= 60 mm and t = 0.025 mm.

4.4 Conclusions

This chapter has presented a new origami stent graft with helical folds. The chapter started with discussions regarding geometric design. Helical folds have been introduced by adjusting the joining position of the two edges of a sheet that had been symmetrically jointed in Chapter 3. The main advantage of the helical folds over the symmetric ones is that they improve the radial strength of the stent graft and ease of the deployment process by synchronizing the deployment of each element.

Geometric properties such as the helical angle and the radius of the helical origami stent grafts during deployment have been calculated. It was found that a larger value for the element number m in one complete circumference of a helix led to a more compact folding of the stent graft with helical folds

The optimum locations for the helical folds are identified by considering both the geometric aspects of folding and the buckling patterns of a thin-walled tube under torsion, which have been found using analytical solutions. Physical models of the tube with prefabricated folds have been produced and then twisted by applying torques at both ends. The models confirm that the tube with the helical folds resembling buckling patterns could be folded more easily under torsion, and with less material damage to the cylinder. Recommendations about helical folds are given for the design of a stent graft.